

Bimetallic Fe/Al-MOF for the Adsorptive Removal of Multiple Dyes: Optimization and Modeling of Batch and Hybrid Adsorbent-river Sand Column Study

Hemant Singh

IIT Kharagpur: Indian Institute of Technology Kharagpur

Sankalp Raj

IIT Kharagpur: Indian Institute of Technology Kharagpur

Rishi karan singh rathour

IIT Kharagpur: Indian Institute of Technology Kharagpur

Jayanta Bhattacharya (✉ jayantaism@gmail.com)

Indian Institute of Technology Kharagpur <https://orcid.org/0000-0001-8644-2915>

Research Article

Keywords: Bimetallic Metal-Organic Framework, Adsorption modelling, hybrid sand-adsorbent, Fixed-bed column, Dyes adsorption, Rhodamine B adsorption

Posted Date: December 22nd, 2021

DOI: <https://doi.org/10.21203/rs.3.rs-1128193/v1>

License:  This work is licensed under a Creative Commons Attribution 4.0 International License.

[Read Full License](#)

1 **Bimetallic Fe/Al-MOF for the adsorptive removal of multiple dyes: Optimization and**
2 **modeling of batch and hybrid adsorbent-river sand column study**

3
4 Hemant Singh ^a, Sankalp Raj ^a, Rishi Karan Singh Rathour ^{a,b}, Jayanta Bhattacharya ^{a, c, d *},

5 ^a School of Environmental Science and Engineering, Indian Institute of Technology

6 Kharagpur, India

7 ^b IPE Global Limited, New Delhi, India

8 ^c Department of Mining Engineering Indian Institute of Technology Kharagpur, India

9 ^d Zelence Industries Pvt. Ltd., India

10
11
12
13
14
15
16
17
18
19
20
21
22
23
24
25
26
27
28
29

30 **Corresponding Author:**

31 Jayanta Bhattacharya (jayantaism@gmail.com , jayantab@mining.iitkgp.ernet.in)

32 **Abstract**

33 Bimetallic Metal organic framework (MOF) has garnered interest over the years with its
34 application in various environmental remediation. In this study, Fe-Al-1,4-Benzene di-
35 Carboxylic acid (FeAl(BDC)) MOF was synthesized, and adsorptive removal of Rhodamine
36 B dye in batch and unique hybrid FeAl (BDC)-River sand fixed-bed column was achieved.
37 The experimental data from the batch studies corroborated well with the Pseudo second-order
38 (PSO) and Freundlich adsorption isotherm models. Furthermore, a fixed-bed column study
39 was conducted to assess the effect of varying flow rate (2, 5, 8 mL/min), bed height (5, 9, 13
40 cm), and feed concentration (10, 20, 30 mg/L) on the adsorption performance of FeAl(BDC)
41 in continuous mode of operation. A uniform mixture of river sand and FeAl(BDC) by weight
42 ratio (9:1) was achieved prior to packing the column. The column study reveals that Sand-
43 FeAl(BDC) can achieve the maximum adsorption capacity of 113.05 mg/g at a flow rate of 5
44 mL/min, feed concentration of 20 mg/L, and bed height of 13 cm. The experimental data of
45 the column study were successfully fitted with BDST, Thomas, Yoon-Nelson, and Dose-
46 response models. The fitting parameter values from the BDST model raise the scope of
47 possible upscaling of the fixed-bed column. Hence, it is proposed that these River sand-
48 FeAl(BDC)-based filters can be widely used in areas facing critical contamination and in
49 poor communities with a high demand for water.

50 **Keywords:** Bimetallic Metal-Organic Framework; Adsorption modelling; hybrid sand-
51 adsorbent; Fixed-bed column; Dyes adsorption; Rhodamine B adsorption

52
53
54
55
56
57
58
59
60
61

62 **1. Introduction**

63 Synthetic dyes are ubiquitous for their use as colouring compounds in textiles, food
64 processing, leather accessories, paper and plastics, cosmetic, printing, and cell staining agents

65 in biological studies (Amini et al. 2011; Yadav and Tyagi 2011; Charumathi and Das 2012).
66 Large portions of these dyes, after use and application, are finally drained to various water
67 bodies and remain there as persistent pollutants and toxicants. They cause multiple
68 irreversibly detrimental effects on the aquatic life by introducing various toxicity; their
69 suspension in water restricts sunlight entry and thus photosynthesis process, and lead to
70 disruption of food chain also influencing human health. Though largely unknown to the
71 current science many of such dyes are known carcinogenic, non-biodegradable in nature, and
72 initially cause discomfort and irritation to skins and eyes, and when inhaled, severe
73 discomfort in the respiratory tract (Charumathi and Das 2012; Nagaraja et al. 2012; Tiwari et
74 al. 2015; Lellis et al. 2019; Geetha Malini et al. 2020). They pose severe challenges to
75 conventional public water treatment systems as they can escape standard treatment schemes.
76 The presence of these dyes in water bodies is a well recognized nuisance and problematic to
77 the aesthetics (Aksu and Tezer 2005; Gupta and Suhas 2009). Many of them are highly stable
78 and can resist biological degradation over a long time. A study estimates almost 10-15 % of
79 unused dyes are released as effluents, and many find ways to water systems from the
80 disposed substances (Kiran et al. 2006; Saini 2017). The organic dye used for the detailed
81 experiments is Rhodamine B. It is a well-known cationic fluorescent, highly water-soluble
82 xanthene dye. It is one of the most predominantly used dyes and has found its application in a
83 variety of research and industrial fields. But due to its high stability, it may also end up as a
84 pollutant in the natural environment (Richardson et al. 2004; Lu et al. 2012; Nagaraja et al.
85 2012).

86 Several biological, physical, and chemical techniques for dye removal from water have been
87 in use. Out of all these, the predominant techniques are adsorption and catalysis. Adsorption
88 is advantageous over catalysis, as the pollutants are transferred between two phases rather
89 than producing unfavorable degradation byproducts (Chegeni et al. 2021). Many other
90 methods have not been popular because of the high cost involved, and lack of feasibility and
91 reliability as well as new environmental impacts, difficulty in using and disposing them.
92 There is relentless research for developing efficient materials for dye removal by adsorption
93 (Robinson et al. 2001; Chen and Chen 2009).

94 Metal organic framework (MOF) is a combination of nodes and linkers, inorganic (metal ions
95 or clusters/SBUs (Structure building units)) and organic in nature. Such materials belong to a
96 class of coordination polymers (Yaghi et al. 2003). Metal organic frameworks are a well-
97 known class of crystalline and porous 2D,3D structures formed with nodes and organic
98 bridges (Gangu et al. 2016; Seth and Matzger 2017).

99 MOF offers a variety of engineering features like high porosity, high surface area, synthesis
100 in mild conditions, facile modification, predictable structures, and fine-tuning for the desired
101 applications (Joseph et al. 2019; Chakraborty et al. 2021). Hence, the applications of MOF
102 are seen in adsorption, catalysis, gas separation by capture, gas storage (hydrogen/ methane),
103 drug delivery, biological imaging, and sensing (Li et al. 2020). MOFs are increasingly being
104 considered for the catalytic or adsorptive removal of inorganic metal cations, inorganic acids,
105 oxyanions/ cations, nuclear wastes, inorganic anions and organic-pharmaceuticals and
106 personal care products, artificial sweeteners and feed additives, agricultural products, organic
107 dyes and industrial products. These are those contaminants that may commonly drain into the
108 wastewater and water systems for consumption of human and animals (Mon et al. 2018).
109 The ease of tuneability of MOF structures with varying metals and ligands for desired
110 application has prompted researchers to explore the field of the multi-metallic and multi-
111 ligand structures of MOFs. Bimetallic MOFs also have the ability to exploit the properties of
112 both the metals bound into same structure by a common ligand or organic linker(Botas et al.
113 2010). Bimetallic MOFs have been found to be more efficient in adsorption, catalysis,
114 semiconducting, gas separation, and storage than their precursor MOFs(Jiao et al. 2017). It
115 has also been observed that many of such structures have good thermal and water stability,
116 making them ideal for wastewater treatment (Li et al. 2019a; Masoomi et al. 2019). Another
117 attractive property of bimetallic MOFs is their poor or low crystallinity. This provides site
118 defects, locally distributed crystallinity, disorders in long-range in crystal structures imparting
119 more sites for action (Li et al. 2019b; Wu et al. 2021).
120 In this study, we have synthesized a bimetallic Iron-Aluminium-Benzene-1,4-dicarboxylic
121 acid (Fe/Al (BDC)) (Chatterjee et al. 2021) MOF by a cost-effective hydrothermal synthesis
122 method. The aim is to use the material to observe the adsorption behaviour of Rhodamine B
123 dye in batch and effectively in the unique hybrid FeAl(BDC)-River sand fixed-bed column
124 simulated filtration process. The adsorbent has also been tested on multiple dyes i.e.
125 Malachite green (MG), Methylene blue (MB), Crystal violet (CV), and Methyl orange (MO)
126 to asses its applicability and potential on other dyes. The adsorbent material FeAl(BDC) was
127 used alongside river sand in the fixed-bed column study. This was carried out to improve the
128 efficacy of the material and, most importantly, to replicate a simple water filtration unit's
129 mechanism. The control studies have also been conducted to ensure the potential of
130 FeAl(BDC) for various applications.

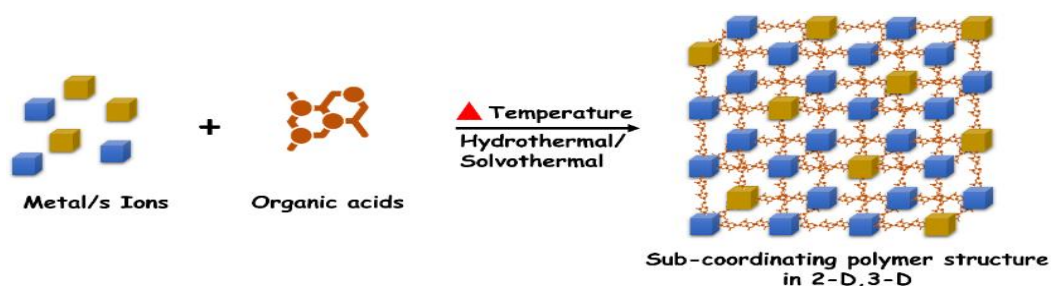
131 **2. Experimental section**

132 **2.1. Chemicals**

133 Ferric Nitrate Nonahydrate ($\text{Fe}(\text{NO}_3)_3 \cdot 9(\text{H}_2\text{O})$), Aluminum Nitrate Nonahydrate
134 ($\text{Al}(\text{NO}_3)_3 \cdot 9(\text{H}_2\text{O})$), Terethalic acid (i.e. Benzene-1,4-dicarboxylic acid or BDC,
135 $\text{C}_6\text{H}_4(\text{CO}_2\text{H})_2$), Dimethylformamide (DMF), Nitric acid (HNO_3) were bought from Merck,
136 India. Various dyes like Malachite green (MG), Methylene blue (MB), Crystal violet (CV),
137 Rhodamine B (RhB) and Methyl orange (MO) were also obtained from Merck, India and
138 used as supplied. Sand was obtained from Ganges river sediment deposits in upstream of
139 Kanpur, India. Deionized (DI) water, conductivity 18 $\text{M}\Omega/\text{cm}$ was used throughout in this
140 study.

141 **2.2. Synthesis**

142 The bimetallic $\text{FeAl}(\text{BDC})$ MOF was synthesized by the solvothermal method. In detail,
143 Ferric Nitrate Nonahydrate (0.001 moles), Aluminium Nitrate Nonahydrate (0.001 moles)
144 and BDC (0.002 moles) were completely dissolved in 65 ml of DMF. The obtained solution
145 was placed in a 100 mL Teflon lined hydrothermal autoclave and was subjected to heating at
146 180 °C for 24 hours. The as obtained yellowish-white precipitate denoted as $\text{FeAl}(\text{BDC})$ was
147 filtered and washed with Ethanol, followed by DI water to remove unreacted components.
148 Finally, the product was dried in a vacuum oven overnight at 60 °C and stored in glass vial
149 for further studies. The river sand was manually cleaned, washed with DI water for upto 5
150 times to remove any dirt or floating materials. It was then left in 10% HNO_3 solution for 48 h,
151 to remove any unwanted impurities in the sand. The sand was then again washed to obtain
152 neutral pH, dried and kept in closed container for further use.



153

154

Fig 1. *The basic concept of Metal-organic framework synthesis*

155

156 **2.3. Characterization of $\text{FeAl}(\text{BDC})$ MOF**

157 The X-Ray diffraction (XRD) patterns of the adsorbent were acquired using X'Pert Powder
158 (PAN analytical instrument) within constraint 2θ between 5 to 80°, Cu- $\text{K}\alpha$ radiation
159 ($\lambda = 1.5405 \text{ \AA}$), and scan rate of 2° min^{-1} at room temperature. Scanning Electron

160 Microscope (SEM) from Carl-Zeiss MERLIN - GEMINI-2, was used to obtain micrograph of
161 the powder adsorbent sample along with Energy Dispersive X-Ray Analysis (EDX). The
162 FTIR spectra by Thermofisher (Nicolet 6700) analyzed thin pellets of the adsorbent material
163 and exhausted adsorbent material mixed with KBr powder in the spectral range of 400–
164 4000 cm⁻¹. Thermogravimetric analyzer (TGA) (NETZSCH technology, USA) was used to
165 analyze thermal stability of the adsorbent material, placed in a platinum crucible, heated from
166 30 to 900 °C at 10 °C/min rate in continuous nitrogen flow (100 mL/min). The UV-
167 vis spectrophotometer of Shimadzu (Model UV-1900) was used for the spectroscopic study
168 of dye. Adsorbent characteristics at different pH were examined in Zeta potential analyzer
169 (Malvern zeta-sizer nano ZS90) at room temperature.

170 **2.4. Batch adsorption studies**

171 To understand the behaviour of the adsorbent-adsorbate, and the adsorption mechanism, as
172 suggested in various literature, pH, amount of dose, stirring speed, and different
173 concentrations were studied. These studies include optimizing single parameters followed by
174 kinetic, particle diffusion, isotherm, and thermodynamics studies for batch experiments.
175 Plastic P.P. (polypropylene) bottles of 100 mL were used for batch adsorption. Initially, 25
176 ppm RhB solution was stirred with 1 g/L of dose in multiple sets. At fixed time intervals, the
177 bottles were collected and analyzed for RhB concentration via UV spectrophotometer. It was
178 observed that equilibrium time was around 90 minutes, with more than 50% reduction within
179 10 minutes. The pH was investigated in the 3-8 range. The stirring speed effect was studied
180 in the range of 200 to 800 rotations per minute (RPM). Dose study was carried out in the
181 range of 0.2 g/L - 2.5 g/L with constant RPM and fixed concentration of 25 mg/L. Dose
182 kinetics was also studied for 0.8, 1, and 1.2 g/L doses. Concentration studies were carried out
183 on 10, 25 and 50 mg/L of RhB and temperature studies for isotherm was carried out at 30, 40
184 and 50 °C after optimization of all single parameters. Adsorption percentage or percentage
185 removal was calculated by Eq(1). Similarly, adsorption capacities at any time and at
186 equilibrium was calculated from Eq (2) and Eq (3). The post experiment calculation was
187 obtained by equations below:

$$188 \quad \%R = \frac{C_0 - C_e}{C_0} \times 100 \quad (1)$$

$$189 \quad q_e = \frac{C_0 - C_e}{W} \times V \quad (2)$$

$$190 \quad q_t = \frac{C_0 - C_t}{W} \times V \quad (3)$$

191 Adsorption capacity and % removal or efficiency were calculated by above formula. ‘R’ is
 192 the % removal, ‘C_e’ and ‘C_o’ are final and initial concentrations, respectively. Adsorption
 193 capacities are denoted by ‘q_e (mg/g)’ at equilibrium and q_t (mg/g) at any given time ‘t’. ‘V’
 194 and ‘m’ are volume in litres and mass of adsorbate in gram, respectively.

195 2.5. Column Adsorption studies

196 Fixed-bed column studies were conducted in an upward flow mechanism with the help of a
 197 peristaltic pump (Miclins, Model no. pp-302CEX) in order to replicate constant flow. Flow
 198 rate (2, 5 and 8 mL/min), Bed height (5, 9 and 13 cm) and concentration (10, 20 and 40
 199 mg/L) studies were conducted along with regeneration of the material in the column.
 200 Although experiments were conducted at room temperature, and RhB dye pH (5.38) was not
 201 changed, as mentioned earlier. The column used was fabricated from a borosilicate glass
 202 column of 1.5 cm in diameter and 20 cm in height.

203 FeAl(BDC) MOF was packed into column with proportion of sand in ratio 1:9 respectively.
 204 Sand and FeAl(BDC) MOF were mixed uniformly and no chemical interaction or bonding
 205 was intentionally obtained (Table1). This was executed in order to attain good hydraulic
 206 conductivity and limit blockage throughout the packed column bed, to lent maximum
 207 retention time for the liquid to pass through the material so that, adsorbent is used to its peak
 208 potential. Hence, for reference, 1 g of material and 9 g of sand mixed together, occupied a
 209 depth of 13 cm in the above-mentioned column. Glass wool (4cm at bottom as support and 3
 210 cm on top as plug) was used to pack the material and restrict any movement inside the bed.
 211 This modification gave EBCT i.e. empty bed contact time of 7.855, 3.142 and 1.96375 min
 212 for flow rate of 2, 5 and 8 mL/min respectively. The ratio of FeAl(BDC): Sand is reported in
 213 Table 1.

214

Table 1. *FeAl(BDC) MOF and Sand ratio in bed depths*

Bed Depth Study	5cm	9cm	13cm
Sand	3.46 g	6.23 g	9 g
FeAl(BDC)	0.38 g	0.69 g	1 g
Total adsorbent used	3.84 g	6.92 g	10 g

215 Total volume passing through the column over time ‘t’ was calculated by Eq (4). Similarly,
 216 total mass (m_{total}) was calculated using Eq (5). The adsorption capacity (q_{total} and q_{eq}) were
 217 calculated using Eq. (6) and (7). The contact time between adsorbate and adsorbent (EBCT) ,
 218 % Removal and Mass transfer zone (MTZ) was calculated using Eq. (8) (9) and (10)
 219 respectively (Cruz-Olivares et al. 2013).

$$220 V_{\text{eff}} = Q * t_{\text{total}} \quad (4)$$

$$m_{\text{total}} = (C_0 * Q * t_{\text{total}})/(1000) \quad (5)$$

$$q_{\text{total}} = \frac{Q}{1000W} \int_0^{t_{\text{total}}} (C_0 - C_t) dt \quad (6)$$

$$q_{\text{eq}} = \frac{q_{\text{total}}}{W} \quad (7)$$

$$\text{EBCT} = \frac{Z * S}{Q} \quad (8)$$

$$\%R = \left(\frac{q_{\text{total}}}{m_{\text{total}}} \right) * 100 \quad (9)$$

$$\text{MTZ} = Z \left(1 - \frac{t_b}{t_{\text{sat}}} \right) \quad (9a)$$

Where, C_0 and C_t (mg/L) are the concentration at inlet and outlet respectively. Q (mL/min) is flow rate. Z (cm) is height and is the cross-sectional area for the fixed-bed column. W (g) represents weight of the adsorbent i.e. FeAl(BDC) MOF and ' t_{total} ' (min) is overall flow time.

3. Results and discussion

3.1. Characterization of FeAl(BDC) MOF

3.1.1. Scanning electron microscopy

The morphology of the FeAl(BDC) was observed (Fig 2), and EDS was obtain for elemental mapping of the sample. Images at high magnification (scale bar 200 nm) clearly show the formation of two differentiable but inseparable rod /bar-like crystal structures. These crystals tend to aggregate and closely overlap each other, with one type of crystal clearly bigger than the other. EDS analysis shows the composition of MOF as Al, Fe, C, O, N in the sample. Moreover, the homogenous distribution of the elements mentioned above is confirmed in the elemental mapping of the FeAl(BDC) MOF. Both MIL53(Fe) and MIL53(Al) findings were correlated with synthesized adsorbent in the Paper (Du et al. 2011; Ai et al. 2014; Li et al. 2015; Pu et al. 2018; Amirilargani et al. 2019).

3.1.2. Powder X-Ray diffraction (PXRD)

PXRD scan for FeAl(BDC) (Fig 3.a.) reveals major multiple sharp peaks conforming formation of MOF and similar to those of MIL-53(Fe) at 9.26, 9.87, 19.65, 20.88, 31.73, 32.55 and 9.07, 18.92, 23.60, 26.52, 33.55, 43.04 with MIL-53(Al). It is to be noted that the synthesized MOF has lower crystallinity than its precursors and the findings were similar in literature (Ai et al. 2014; Li et al. 2015; Pu et al. 2018; Amirilargani et al. 2019).

3.1.3. FTIR-Fourier transform infrared spectroscopy

The characteristic peaks obtained in FTIR spectra (Fig 3 b) for FeAl(BDC) have significant peaks at 577 cm^{-1} and 1014 cm^{-1} , attributed to Fe-O and Al-O bonds, respectively. The broadened peak at 3405 cm^{-1} points towards stretched vibrating hydroxyl group. Series of

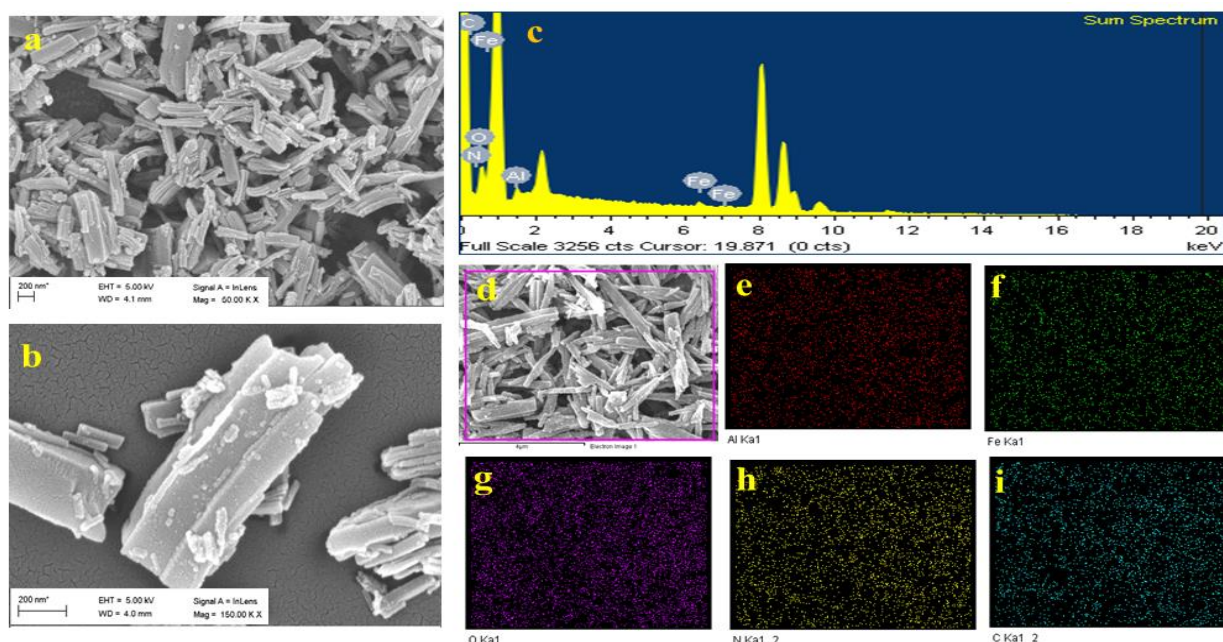
252 peaks for Carboxylate groups stretching can be observed in the spectra with signature peaks
253 at 1577 (asymmetric) and 1405 (symmetric) cm^{-1} , followed by C-H bond vibration for
254 benzene at 750 cm^{-1} coming from dicarboxylate in BDC. C=C an aromatic bond vibration
255 may depict the adsorbed RhB onto the adsorbent in range 1528 to 1542 cm^{-1} , which only
256 appears in spent FeAl(BDC) (Banerjee et al. 2012; Vu et al. 2015; Yan et al. 2015; Postai et
257 al. 2016).

258 **3.1.4. TGA- Thermogravimetric analysis**

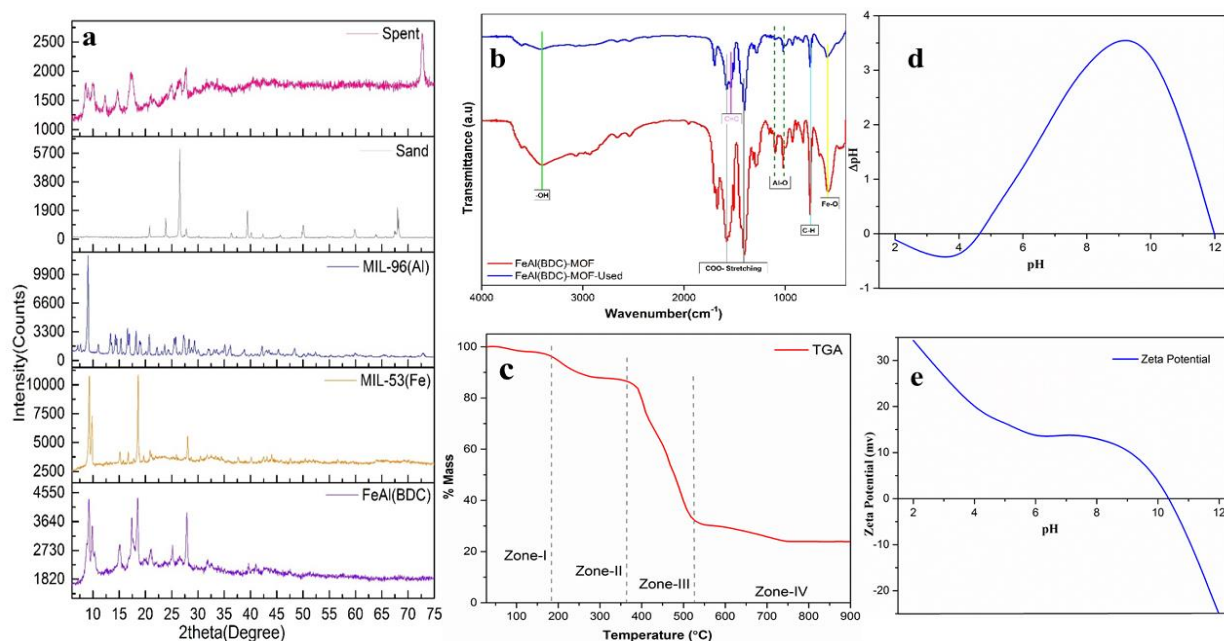
259 Zone I and Zone II (Fig. 3c) depict initial weight loss occurring below 200 °C with the
260 removal of water from the sample's surface, possible decomposition of DMF from pores, and
261 stranded organic linker molecule. However, in zone III (Fig. 3c), very steep weight loss (
262 400- 550 °C) is observed due to the rapid decomposition of the terephthalate linker leading to
263 the breakdown of MOF structure. The stability of the sample is less as compared to, but can
264 be attributed similar to, combined properties of MIL-53(Al, Fe). Zone IV (Fig. 3c) depicts the
265 formation of amorphous products, and weight loss is almost stable (Qian et al. 2013; Mishra
266 et al. 2014)

267 **3.1.5. Zeta Potential**

268 The Zeta potential and isoelectric point were obtained by adjusting the pH of DIW to 2, 4, 6,
269 7, 8, 10, and 12 with sodium hydroxide and nitric acid. 10 mg of sample was dispersed in 25
270 ml of the maintained pH solution. The final pH of the solution was measured after 2 and 12
271 hrs. ΔpH was calculated by measuring the difference between initial and final pH. The plot
272 between Initial pH and ΔpH (Fig. 3 d) showed an isoelectric point around 5 pH. The
273 adsorbent has a negative surface charge at acidic pH, and the charge increases with an
274 increase in pH to the basic range. Hence, RhB and FeAl(BDC) adsorption mechanisms may
275 favor electrostatic interaction (Zarenezhad et al. 2021).



276 **Fig 2.** *a and b are Micrograph of FeAl(BDC)MOF at 200 nm scale. c,d,e,f,g,h,i are*
 277 *Elemental mapping of FeAl(BDC) MOF for elements and distribution of Al, Fe, O, N, C*
 278 *respectively.*



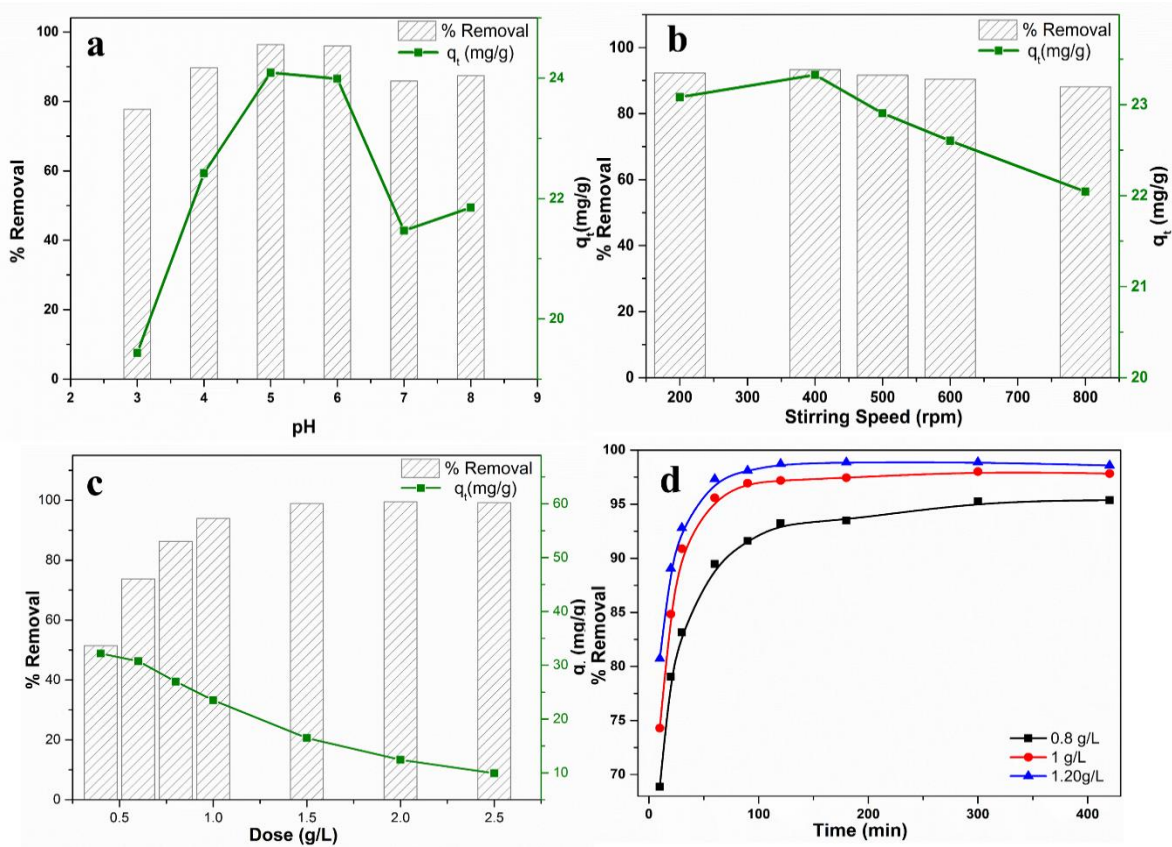
279 **Fig 3.** *a. PXRD peak data for spent(after adsorption), Sand(Column), MIL-53(Al), MIL-*
 280 *53(Fe), FeAl(BDC), b. FTIR spectra for adsorbent and spent FeAl(BDC), c.*
 281 *Thermogravimetric analysis(TGA), d. Isoelectric point measurement for FeAl(BDC), e. Zeta*
 282 *Potential measurements*

283

284 **3.2. Batch Study**

285 **3.2.1. Optimization of factors affecting adsorption: pH, RPM & adsorbent dose**

286 The study for pH was carried out at room temperature for pH 3, 4, 5, 6, 7, 8. At pH of 5 & 6,
287 97-99% removal of RhB was observed. It was observed that with the increase in OH⁻ ions
288 RhB adsorption decreased, which can be attributed to the change of surface charge on
289 adsorbent material with increased pH. It should be noted that RhB solution's pH stayed
290 around 5.36±0.2; hence, no change to pH was carried out for further experiments (Fig 4a). A
291 stirring speed study was optimized for a fixed dose of 1 g/L and 25 mg/L of dye
292 concentration for 90 minutes (Fig 4b). Dose study was carried out at an optimum
293 concentration of 25mg/L of RhB for 90 minutes with adsorbent dose variation of 0.5-2.5
294 mg/L. It was observed that at doses of 0.9, 1, 1.50 g/L, the adsorbent attained more than 90%
295 removal efficiency (Fig 4c). It was also observed that 70-75% of the removal was obtained in
296 the first 5 min of the experiment and 85-90% within 20 minutes of contact. Adsorption
297 gained 99% efficiency within 90 minutes and reached saturation after that due to blockage or
298 saturation of the adsorption sites. The experiment was extended to few more hours to observe
299 desorption if any. The initial concentration of 10, 20, 30, 40, 50 and 60 mg/L and fixed
300 adsorbent dose of 1 g/L efficiency was investigated. The rate of removal increased upto 50
301 mg/L, but limited adsorbent dose saturated quickly with higher concentration. Hence, no
302 significant removal was observed beyond 50 mg/L.



303

304 **Fig 4. a.** %Removal v/s pH, **b.** %Removal v/s RPM, **c.** % Removal v/s Dose, **d.** % Removal v/s
 305 dose, kinetics for 0.8, 1, 1.2 g/L., Conditions: $C_o = 25$ mg/L, Time = 90 minutes, pH = 3-8,
 306 Dose = 0.4-2.5 g/L, and Temperature = 30 °C, Stirring speed = 200±20 rpm.

307

308 3.2.2. Kinetics based on the concentration

309 The kinetic study determines the adsorption rates and evaluates the different optimized
 310 conditions for further study (Fig 5). A kinetic study was conducted, with optimum dose and
 311 concentration for a maximum time of 420 min. For a better understanding of the experiments,
 312 nonlinear equations are used. Kinetics at RhB concentration (10, 25 and 50 mg/L) was
 313 studied by Pseudo first order (Eq.10), Pseudo second-order (Eq.11), Elovich model (Eq.12)
 314 and Intraparticle diffusion model (Eq.13)(Wang and Guo 2020a).

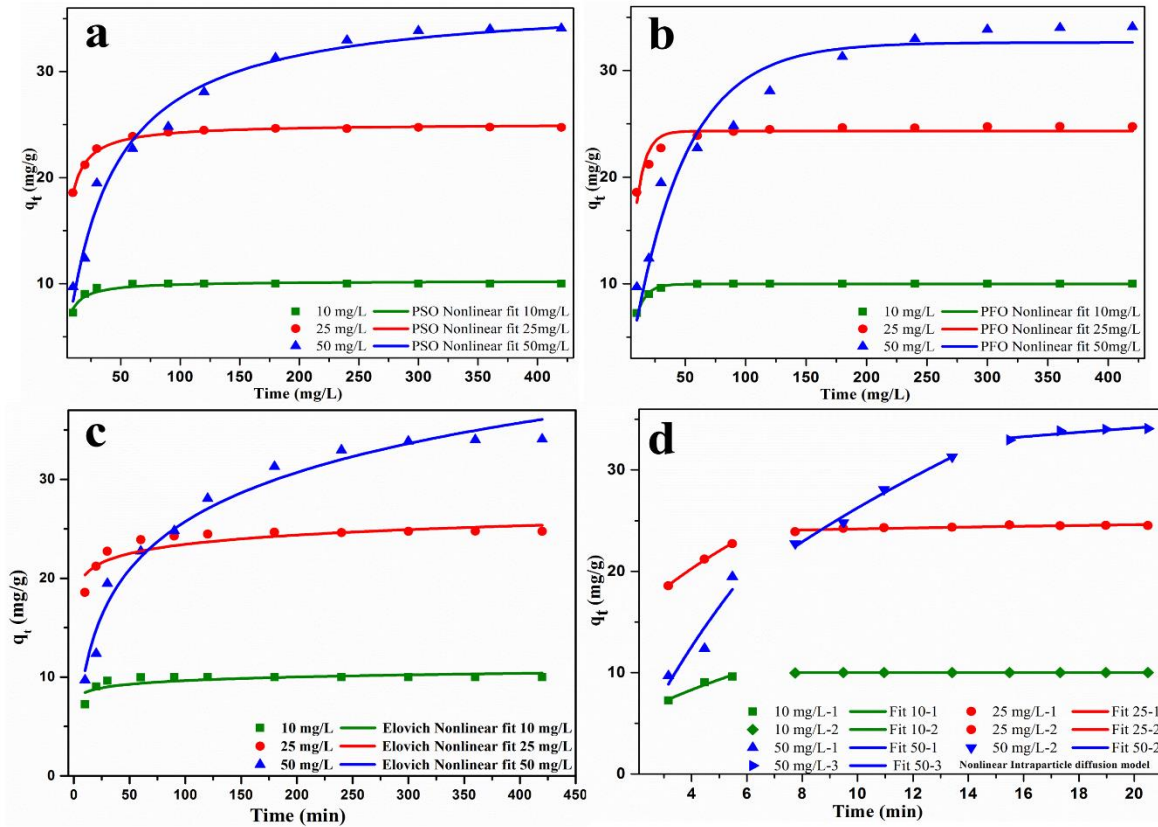
$$315 \quad q_t = q_e(1 - \exp(-k_1t)) \quad (10)$$

$$316 \quad q_t = (k_2^2 q_e^2 t) / (1 + k_2 q_e t) \quad \& \quad h = k_2 q_e^2 \quad (11)$$

$$317 \quad q_t = \beta \ln(\alpha \beta t) \quad (12)$$

$$318 \quad q_t = k_{id} t^{0.5} + c \quad (13)$$

319 Where, 'q_t' and 'q_e' are the adsorption capacities at time 't' and at equilibrium with units
 320 (mg/g). k₁ (min⁻¹), k₂ (g/mg min), are the pseudo first-order and the pseudo second-order rate
 321 constants. h (mg/g min), α (mg/g min) are the initial adsorption rate, t is contact time in min, β
 322 (g/mg) is adsorption constant, k_{id} (mg/g min) intraparticle diffusion rate constant, t is contact
 323 time in min, c (mg/g) is constant of any experiment.



324 **Fig 5. a.** PSO nonlinear fit, **b.** PFO nonlinear fit, **c.** Elovich nonlinear fit, **d.** IPD model.
 325 Conditions: C_o = 10, 25, and 50 mg/L, Time = 420 minutes, pH = 5.36 ± 0.2, Dose = 1 g/L,
 326 Stirring speed = 200±20 rpm, and Temperature = 30 °C.

327

Table 2. Kinetic model parameters

C _o (mg/L)	PFO				PSO			Elovich model		
	q _{e, Exp} (mg/g)	k ₁ (min ⁻¹)	q _{e, Cal.} (mg/g)	R ²	k ₂ (g/mg*min)	q _{e, cal.} (mg/g)	R ²	α (g/mg*min)	q _{e, cal.} (mg/g)	R ²
10	10	0.1259	9.97	0.99	0.0289	10.25	0.91	46195	0.52	0.57
25	24.76	0.1289	24.32	0.86	0.0115	25.09	0.99	475018	1.34	0.76
50	34.07	0.0225	32.62	0.93	7.88E-4	36.95	0.97	2.402	7.30	0.97

328

Table 3. Intraparticle diffusion model

C _o (mg/L)	kip1 (mg/g×mi n ^{0.5})	kip2 (mg/g×mi n ^{0.5})	kip3 (mg/g× min ^{0.5})	C _{i1}	C _{i2}	C _{i3}	R ₁ ²	R ₂ ²	R ₃ ²
10	4.292	0.009		-0.28	9.96		0.94	0.26	
25	7.415	0.318		5.42	23.17		0.99	0.75	
50	16.678	10.038	1.823	-20.8	-5.48	25.98	0.74	0.97	0.72

329

330 The PSO model parameters fits better with experimental data and R² ranges from 0.91, 0.99,
 331 and 0.97 for 10, 25, and 50 mg/L of RhB concentration, respectively as compared to the PFO
 332 model and Elovich model (Table 2). However, the value of ‘q_{e,cal}’ is comparable with the ‘q_e
 333 _{Exp}’ values for PFO and PSO model but inconsistent with values from the Elovich model.
 334 Hence, it can be inferred that, adsorption process was dominated by pseudo second order
 335 kinetics and followed chemisorption mechanism. This also suggests that, adsorption is
 336 occurring at final stage and at multiple active sites on the adsorbent material FeAl(BDC)
 337 (Kadirvelu et al. 2005; Wang and Guo 2020a).

338 Experimental data were further analyzed for intraparticle diffusion (Fig 5e) to gather
 339 information on the adsorptive mechanism (Table 3). The plot between qt v/s t^{0.5} shows the
 340 concentration models, but none of the graphs passes through the origin. The graphs for 10
 341 and 25 mg/L can be set into two stages and 50 mg/L into 3 stages. This suggests that
 342 intraparticle diffusion was not the rate-limiting step. The adsorption may also be occurring
 343 due to bulk diffusion of RhB into the adsorbent material and adsorption-desorption at
 344 equilibrium, determining mass transfer process (Gaaz et al. 2015; Rathour et al. 2020).

345

346 3.2.3. Isotherm parameters study

347 After optimizing various parameters, temperature study was conducted at three scales of 30,
 348 40, 50 °C at concentration (10, 25, 50, 100, 200 mg/L), dose (1g/L) and pH (5.36 ± 0.2).

349 Isotherm models have certain assumptions are to be considered. Langmuir model (Eq. 14)
 350 assumes the possibility of only monolayer adsorption with identical and finite adsorption
 351 sites. This considers homogenous adsorption with a molecule thickness on the adsorbent. The
 352 factor R_L, describes the attractive forces and distance relation in the adsorption process. It
 353 explains the possibility of adsorption as, irreversible below R_L = 0, favourable between 0 <
 354 R_L < 1, linear at R_L = 1, and unfavourable above R_L > 1(Weber and Chakravorti 1974).
 355 Freundlich model (Eq. 15), gains over Langmuir model, as it considers adsorption beyond

356 monolayer and hence, can be applied to multi-layered and heterogeneous adsorption
 357 process(Zaheer et al. 2019; Wang and Guo 2020b). Dubinin-Radushkevich or D-R model
 358 (Eq. 16) was better understood on vapour adsorption on solids with an assumption that pore
 359 distribution on the adsorbent surface followed Gaussian energy distribution(Dąbrowski 2001;
 360 Wang and Guo 2020b). The Temkin model (Eq. 17), similar to the Freundlich model, applies
 361 to multilayer adsorption but ignores the extremely low and high concentration of adsorbate in
 362 the system (Abdi and Abedini 2020; Rathour et al. 2020; Wang and Guo 2020b).

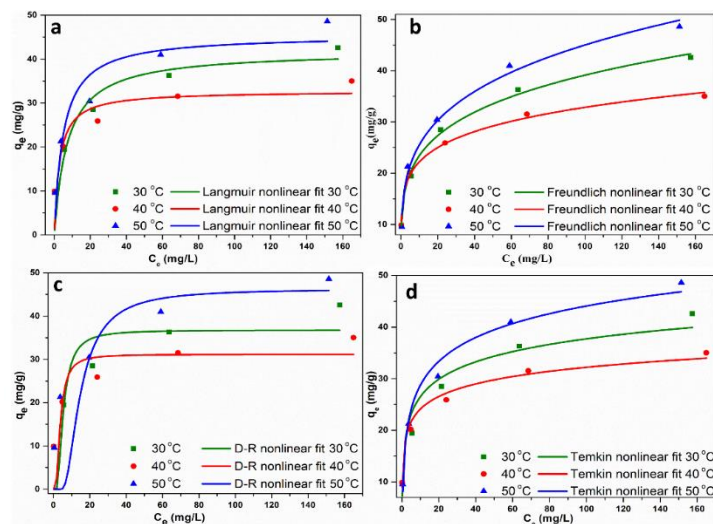
363 Langmuir $q_e = \frac{q_m k_L C_e}{1 + k_L C_e}$ and $R_L = \frac{1}{1 + k_L C_0}$ (14)

364 Freundlich $q_e = k_f C_e^{1/n}$ (15)

365 Dubinin-Radushkevich (D-R) $q_e = q_m \exp\left(-\beta \left(RT \ln \left(1 + \left(\frac{1}{C_e} \right) \right) \right)^2 \right)$ and $E = \frac{1}{\sqrt{2\beta}}$ (16)

366 Temkin $q_e = B \ln(A_t C_e)$ (17)

367 Where C_e (mg/L) is the outlet concentration of RhB in equilibrium time, q_m (mg/g) is the
 368 maximum adsorption capacity, and q_e (mg/g) is the amount of RhB adsorbed per unit weight
 369 of adsorbent. k_L (L/mg) is the energy of adsorption, R_L is the separation factor, k_f ((mg/g).
 370 (L/mg)^{1/n}) is the quantity of RhB adsorbed onto adsorbent for a given equilibrium
 371 concentration, E (K.J./mol) is the free energy in the adsorption process, $\beta \times 10^{-6}$ (mol²/J²) is the
 372 constant related to the sorption energy, ‘ A_t (L/g)’ is the equilibrium binding constant
 373 corresponding to the maximum binding energy. ‘ n ’ is a measure of adsorption intensity, and
 374 B is related to the heat of adsorption.



375
 376 **Fig 6.** Nonlinear fitting curve for Isotherm models **a.** Langmuir, **b.** Freundlich, **c.** Dubinin-
 377 Radushkevich (D-R), and **d.** Temkin model

Table 4. Isotherm models parameters

Temp. (°C)	Langmuir				Freundlich			
	q _m , Exp.	q _m cal.	K _L	R _L	R ²	K _F	1/n	R ²
30	42.59	41.86	0.14	0.035	0.98	14.04	0.22	0.99
40	35.03	32.73	0.35	0.014	0.98	15.06	0.17	0.99
50	48.59	45.47	0.20	0.024	0.97	14.53	0.24	0.98
	Temkin			Dubinin-Radushkevich (D-R)				
	B	At	R ²	q _m cal.	β	E	R ²	
30	42.59	4.86	23.47	0.93	36.76	3.91E-6	3.57E+02	0.66
40	35.03	3.51	96.26	0.97	31.17	1.85E-6	5.19E+02	0.55
50	48.59	6.65	7.51	0.98	46.26	2.40E-5	1.44E+02	0.21

378
379 A comparison of all four models is provided in Table 4, and nonlinear plots are given in Fig
380 6. The Langmuir, Freundlich and Temkin models have R² values in the range of 0.97-0.98,
381 0.98-0.99, and 0.93-0.98, respectively, and have the closest fit to the experimental data over
382 D-R model with R² 0.21-0.66. The calculated adsorption capacity (q_m cal.) from the Langmuir
383 model is comparable with the experimental adsorption capacity. The R_L values for three
384 temperatures are 0.349, 0.0139, and 0.0239 (all 0 < R_L < 1) respectively which is favourable
385 for adsorption. It should be noted that adsorption capacity as an overall increases with
386 increase in temperature, with a significant drop at 40°C and then increased at 50°C. However,
387 the Freundlich model correlates better with the experimental data, followed by Langmuir and
388 Temkin model. It also implies that multilayer, heterogeneous adsorption is dominant.

389

390 3.2.4. Thermodynamic study model

391 Thermodynamic studies on the adsorption process tend to explain the nature of the
392 adsorption. Hence at three temperatures i.e., 30, 40, and 50 °C, ΔG⁰ (Gibbs free energy) was
393 calculated using

394 Eq (18, 19, 20) for adsorption of RhB on FeAl(BDC) MOF.

$$395 \ln(k_c) = \frac{\Delta S^0}{R} - \frac{\Delta H^0}{R} \left(\frac{1}{T}\right) \quad (18)$$

$$396 \Delta G^0 = -RT \ln(k_c) \quad (19)$$

$$397 k_c = m \frac{q_e}{C_e} \quad (20)$$

398 Where, ΔH⁰(J/mol) is the enthalpy change, ΔS⁰ (J/mol. °K) is the change in entropy, ‘k_c’ is
399 the distribution coefficient constant, R is the universal gas constant (8.314 J/Kmol), T is the
400 absolute temperature (°K). ‘m’ (g/L) is the amount of composite, ‘q_e’ (mg/g) is RhB
401 adsorbed at equilibrium and C_e (mg/L) is the equilibrium concentration

402 The adsorption process was spontaneous, as depicted by increasing negative ΔG° values over
 403 the increasing temperature (Table 5). The value also suggested the role of physical adsorption
 404 of RhB onto FeAl(BDC) MOF, as it was less than 40 KJ/mol (Choudhary et al. 2020). The
 405 positive value of ΔH° depicts the endothermic nature of the process whereas positive ΔS°
 406 shows high randomness at the solid-liquid interface and entropy-driven process, which means
 407 adsorbate and adsorbent shows a good affinity towards each other.

408

Table 5. *Thermodynamic parameters*

ΔH° (KJ/mol)	ΔS° (J/mol×K)	ΔG° (KJ/mol)		
		30°	40°	50°
20.186	76.85	- 3.10	- 3.86	- 4.63

409

Table 6. *Comparison of Batch adsorption capacities of FeAl(BDC) towards RhB with other adsorbents.*

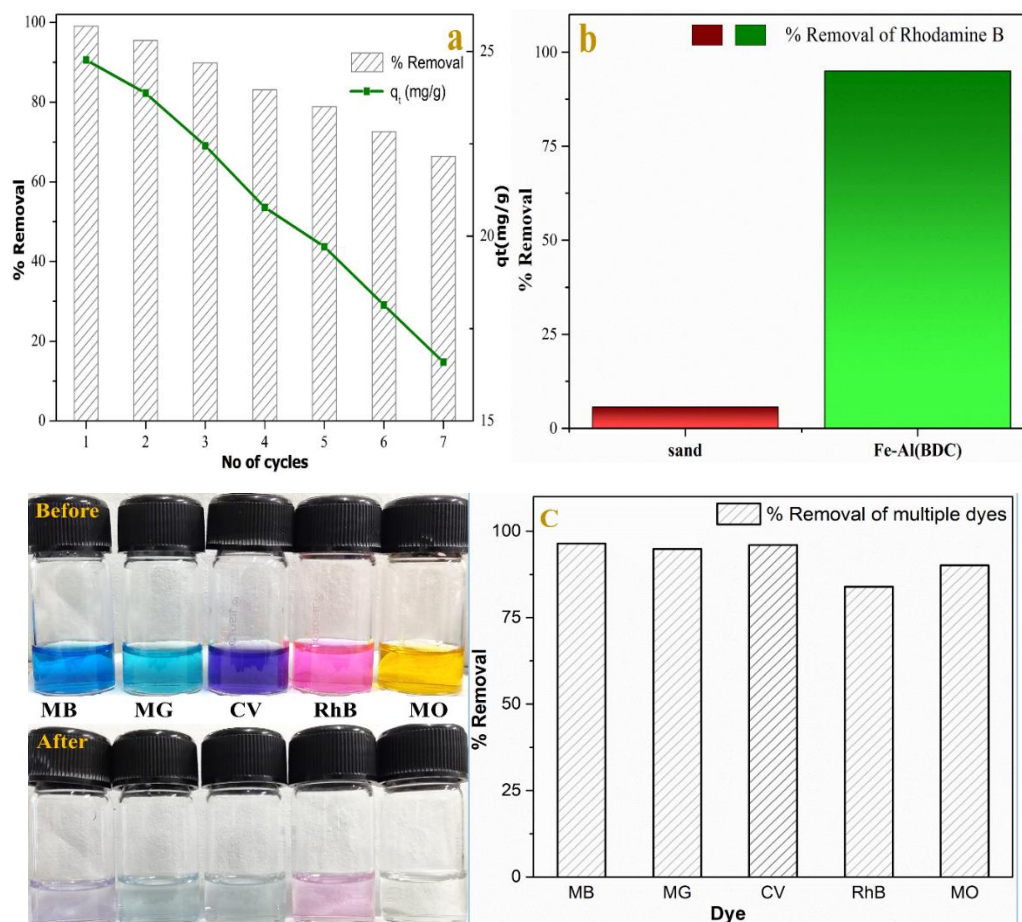
Adsorbent	pH	Eq. time	Initial conc. (mg/L)	qe (mg/g)	Reference
Activated carbon	5.7	150	20	16.12	(Kadirvelu et al. 2005)
GO-PDA/PES-SPES membrane	4.0	180	2-70	26.34	(Wang et al. 2021)
Fe@ZIF-67 (1%)	10	240	20	47.71	(Nazir et al. 2021)
Beta zeolite with SiO ₂ /Al ₂ O ₃	3	60	5	27.97	(Cheng et al. 2018)
MoS ₂	-	120	40	26.18	(Li et al. 2019c)
FeAl(BDC)	5.3	90	25	41.86	PW

410 PW : Present Work

411 3.2.5. Batch desorption, control and multiple dye adsorption study

412 For the Desorption study(Fig 7a), two solutions of Acetone and Ethanol (5M) each were
 413 used. The desorption efficiency was found to be 99% and 98%, respectively, for 20 mg/L
 414 concentration of RhB dye in 30 minutes time. Pure Ethanol (98%) was used for all desorption
 415 studies in batch and fixed-bed column. The adsorbent was removed by centrifugation and
 416 then desorbed in 50 ml ethanol, followed by separation with centrifugation. Each time the
 417 process was followed in a similar manner of adsorption-desorption-DIW wash. The removal
 418 efficiency of the material decreased with each cycle and was observed to drop below 80%
 419 after 5th cycle. Similarly, the adsorption capacity of the material decreased with each cycle.
 420 Overall, the adsorbent material holds good. The loss of various properties can be attributed to

421 the loss of mass of the adsorbent in each cycle and the change in structural crystallinity (Fig
 422 3a. Spent adsorbent XRD). The comparative study of RhB adsorption by sand and
 423 FeAl(BDC) showed negligible adsorption by sand (< 5%) in 90 min. Hence, it can be
 424 deduced that FeAl(BDC) MOF obtains the overall adsorption in the system (Fig 7 b).
 425 Furthermore, the adsorbent ability to remove multiple dyes, namely MG, MB, CV, and MO
 426 was evaluated. It was observed that the removal efficiency for all dyes were above 90%, with
 427 the given dose of 1g/L and 20 mg/L of individual concentration (Fig 7 c).



428

429

430 **Fig 7. a.** Desorption of Rhodamine B from FeAl(BDC) and **b.** Comparative study on sand and
 431 FeAl(BDC) for use in column fixed-bed, **c.** Adsorption of multiple dyes, i.e. MB, MG, CV,
 432 RhB, MO.

433 3.3. Column Study

434 To understand the column adsorption mechanism, parameters affecting Rhodamine B
 435 adsorption on FeAl(BDC) MOF in continuous fixed-bed columns such as flow rate (Q),
 436 fixed-bed height (Z), and inlet concentration (Co) were studied in depth. To further
 437 understand the behaviour, experimental data were correlated and nonlinearly plotted with

438 Thomas, Yoon-nelson, Bed depth-service time (BDST) and dose response (D-R) models and
 439 are given as follows(Han et al. 2008; Cruz-Olivares et al. 2013).

Thomas model

$$\frac{C_t}{C_o} = \frac{1}{1 + \exp\left(\left(\frac{k_{TH} * q_o * W}{Q}\right) - (k_{TH} * C_o * t)\right)} \quad (21)$$

Yoon Nelson model

$$\frac{C_t}{C_o} = \frac{1}{1 + \exp(k_{YN} * (\tau - t))} \quad (22)$$

Bed depth-service time (BDST) model

$$\frac{C_t}{C_o} = \frac{1}{1 + \exp(k_{BDST} * C_o \left(\frac{N_o}{C_o * v} * L - t\right))} \quad (23)$$

Dose-response (D-R) model

$$\frac{C_t}{C_o} = 1 - \frac{1}{1 + \left(\frac{C_o * Q * t}{q_o * X}\right)^a} \quad (24)$$

440 Where C_o (mg/L) is the initial Concentration of RhB, C_t (mg/L) is the Concentration of RhB
 441 at any time 't', q_o (mg/g) is adsorption capacity, t (min) is adsorption time in min, W (g) and
 442 X (g) are the weight of the total adsorbent. Q (mL/min) and v (mL/min) are the flow rates in
 443 column, k_{TH} (mL/min.mg) is the Thomas model rate constant, k_{YN} (h^{-1}) is the Yoon-Nelson
 444 rate constant, τ and (h) is the required time for 50% adsorbate breakthrough. ' k_{BDST}
 445 (L/mg.min)' is rate of mass transfer from liquid to solid. N_o (mg/L) adsorption capacity of
 446 bed, L (cm) and Z (cm) are bed heights, 'a' is constant for Dose-response model.

447

Table 7. Column parameters from design and experiments

Q (mL/ min)	L or Z (cm)	Co (mg/ L)	t _B (min)	t _E (min)	EBC T	MTZ (cm)	m _{total} (g)	V _{eff} (mL)	q _{total} (mg)	q _{eq} (mg/g)	%R
2	13	20	840	1740	5.11	6.72	69.6	3480	44.03	44.03	63.26
5	13	20	780	1740	2.05	7.17	176	8700	113.05	113.05	64.68
8	13	20	240	750	1.28	8.84	120	6000	63.96	63.96	53.30
5	5	20	270	840	0.79	3.69	84	4200	46.43	122.18	55.27
5	9	20	570	1260	1.42	5.2	138	6750	84.35	120.67	61.12
5	13	20	780	1740	2.05	7.17	176	8700	113.05	113.05	64.97
5	13	10	1020	1990	2.05	6.33	99.5	9950	72.62	72.62	72.99
5	13	20	780	1740	2.05	7.17	176	8700	113.05	113.05	64.97
5	13	40	420	960	2.05	7.31	192	4800	109.42	109.42	56.99

448

3.3.1. Study with the varying flow rate

The breakthrough curves (BTC) for feed flow rates at 2, 5, 8 mL/min are shown in the graph, along with various model fittings (Fig 8. a, b, c, and d). The bed height and Rhodamine B concentration were fixed at 13 cm and 20 mg/L, respectively. It was observed that the flow rate had a significant effect on column performance and adsorbent efficiency. The maximum performance from experimental data of the column was obtained at the flow rates of 2, 5, 8 mL/min was 63.26, 64.68, and 53.30% removal efficiency with 44.03, 113.05, and 63.96 mg/g uptake capacity, respectively (Table 6). There was a considerable decrease of % removal and uptake capacity with increasing flow rate.

Further analyzing the graphs, it can be seen that at lower flow rates, the adsorbent material is able to capture dye molecules for a longer duration. When the availability of active sites reduces, the BTC sees a change in slope and reduced capacity. The feed rate provides enough residence time to attract dye molecules on the adsorbent and attain equilibrium. At a higher flow rate, the dye molecule gets very less contact time in the column, and adsorption equilibrium is not attained. This leads to a sudden and steeper rise in the BTC. The mass transfer zone (MTZ) increases at higher feed rates (Table 6). The mass transfer rate leads to faster saturation as the amount of dye molecule captured by unit bed depth increases with increasing flow rate (Saha et al. 2012; Afroze et al. 2016).

3.3.2. Study with the varying bed height

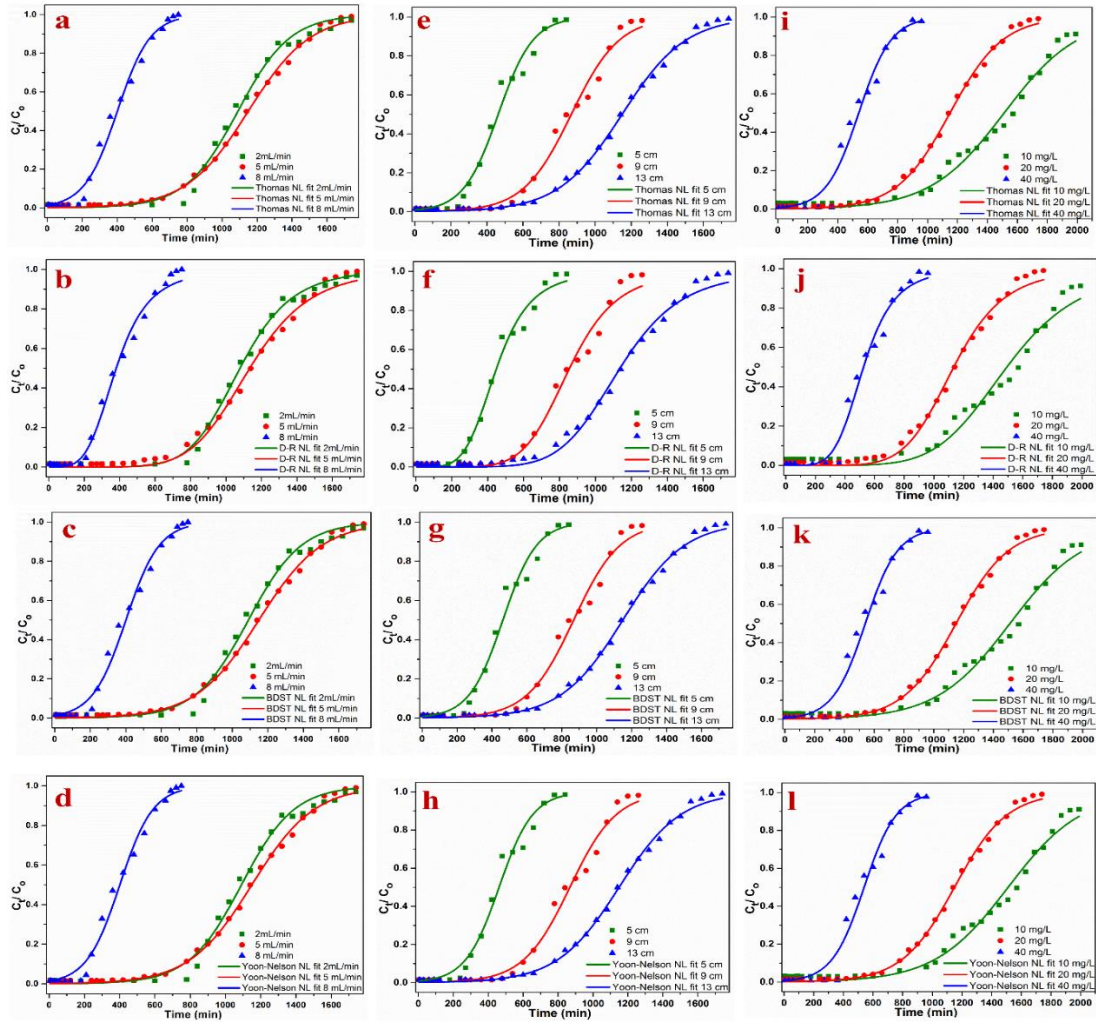
The breakthrough curves for column bed heights and fitted models at 5, 9, 13 cm are shown in the graph (Fig 8. e, f, g, and h). The flow rate and Rhodamine B concentration were fixed at 5 mL/min and 20 mg/L, respectively. The EBCT measured was 0.79, 1.42, and 2.05, respectively. It was observed that variation in bed height had a considerable effect on the removal efficiency of adsorbent. The maximum performance from experimental data of the column obtained at the bed heights of 5, 9, 13 cm was 55.27, 61.12, and 64.97 % removal efficiency with 122.18, 120.67, and 113.05 mg/g uptake capacity, respectively. With the increase in bed height, the removal efficiency increased which is obviously due to the increased mass of adsorbent while the adsorption capacity decreased. The breakthrough time increased with an increase in bed height as 270, 570, and 780 minutes, respectively, which signifies that residence time increased, giving more interaction time between dye and adsorbent (Saha et al. 2012; Afroze et al. 2016).

3.3.3. Study with the varying concentration

The breakthrough curves for Rhodamine B concentration at 10, 20, 40 mg/L and model fits are shown in the graph (Fig 8. i, j, k, and l). The flow rate and bed height were constant at 5 mL/min and 13 cm, respectively. The maximum performance from experimental data of the column was obtained at the flow rates of 2, 5, 8 mL/min was 72.99, 64.97, and 56.99% removal efficiency with 72.62, 113.05, and 109.42 mg/g uptake capacity, respectively. The breakthrough time decreased with increasing concentration, and at higher concentration a sharp rise, and at lower concentration a flattened rise in the BTC was observed. The saturation on active sites on the adsorbent saturated quickly at 40 mg/L, thereby exhausting column earlier than other concentrations (Afroze et al. 2016; Karami et al. 2021).

3.3.4. Model fitting for breakthrough curves

Thomas model (Eq.21) (Table 7) shows a good uptake capacity at lower flow rates but abruptly drops at a higher flow rate. This sudden drop is observed across all the models and is consistent with the experimental data. It can be explained by residence time, which is not sufficient at a higher flow rate for adsorbate-adsorbent interaction. The K_{TH} value of this model decreases with an increase in depth (i.e., increase in adsorption sites) of the fixed-bed, and hence a longer breakthrough time is observed. The Yoon-Nelson model (Eq.22) (Table 7) rate constant K_{YN} also drops similar to K_{TH} with an increase in bed height. The ' t_b ' (Table 6) of experimental data was also comparable to τ . The value of τ increases with the increase in bed depth (EBCT rises), and hence similar pattern is observed as the Thomas model. Bed depth-service time (BDST) model (Eq.23) (Table 8) fitting has better representation of parameters to support an upscale of the continuous fixed-bed column (Babazadeh et al. 2021). With the increase in bed height the ' K_{BDST} ' decreases while the value of ' N_o ' has little variation. Dose Response (D-R) model (Eq.24) (Table 8) uptake capacity was similar to that of Thomas model in all the fixed-bed running conditions. All the above findings were similar in various literatures (Cruz-Olivares et al. 2013; Afroze et al. 2016; Podder and Majumder 2016; Karami et al. 2021).



510

511 **Fig 8.** Flow rate (a to d), bed height (e to h), and concentration (i to l) variation modelled on
 512 a, e, and i. Thomas model, b, f, and j. Dose-Response model, c, g and k. BDST model, d, h
 513 and l. Yoon-Nelson model respectively (Conditions : Flow rate: $Q = 2, 5, 8$ mL/min, $C_o = 20$
 514 mg/L, $Z = 13$ cm, $m = 1$ g, Bed height: $Z = 5, 9, 13$ cm, $m = 0.38, 0.69, 1$ g, $Q = 5$ mL/min, $C_o =$
 515 20 mg/L, Rhodamine B concentration: $C_o = 10, 20, 40$ mg/L, $Z = 13$ cm, $m = 1$ g, $Q = 5$ mL/min)

Table 8. Experimental data fitting on Thomas model and Yoon-nelson Model

Column parameters				Thomas model		Yoon-nelson Model		
Q (mL/min)	Z (cm)	C_o (mg/L)	W (g)	$K_{TH} \times 10^{-4}$ (mL/mg \times min)	q_0 (mg/g)	R^2	K_{YN} (1/min)	τ (min)
2	13	20	1	3.34	43.61	0.99	0.00669	1090
5	13	20	1	2.82	114.94		0.00565	1149
8	13	20	1	5.31	64.13		0.01062	401
5	5	20	0.38	5.17	121.69	0.98	0.01035	462
5	9	20	0.69	3.75	125.75		0.00751	868
5	13	20	1	2.82	114.94		0.00565	1149
5	13	10	1	4.04	75.568	0.98	0.00405	1511

5	13	20	1	2.82	114.94	0.00565	1149
5	13	40	1	2.29	108.02	0.0092	540

516

517 Data for BDST and Dose-Response is given below in table

Table 9. Experimental data fitting on Bed depth-service time (BDST) model and dose-response model

Column parameters				Bed depth-service time (BDST) model			Dose-Response model		
Q (mL/min)	Z (cm)	Co (mg/L)	W (g)	KBDST x10 ⁻⁴ (mL/mg.min)	No (g/L)	R ²	q ₀ (g/L)	a	R ²
2	13	20	1	3.34	4247	0.99	43	7.35	0.99
5	13	20	1	3.30	9555		113	6.59	
8	13	20	1	5.31	6245		61	4.12	
5	5	20	0.38	5.17	11708	0.98	118	4.68	0.98
5	9	20	0.69	3.75	12204		124	6.43	
5	13	20	1	2.82	11192		113	6.59	
5	13	10	1	4.04	7358	0.97	75	5.98	0.97
5	13	20	1	2.82	11192		113	6.59	
5	13	40	1	2.29	10518		105	4.98	

518

519

520 3.3.5. Column regeneration study

521 Column regeneration was performed for up to 3 runs, and conditions were followed similar to
522 batch study. The study was conducted at a fixed condition of 20 mg/L concentration of RhB,
523 5ml/min of flow rate, adsorbent dose of 0.38 g, i.e. 4 g with sand and 5 cm of column height.
524 The column was run continuously for the study without breaking the cycle of adsorption-
525 desorption-DIW wash and without removing the adsorbent from the column. An average plot
526 is given in graph fig 9. It can be observed that rapid desorption occurs within 10 minutes of
527 the process. The desorption process starts attaining saturation after 40 minutes of continuous
528 run, and no considerable desorption occurs.

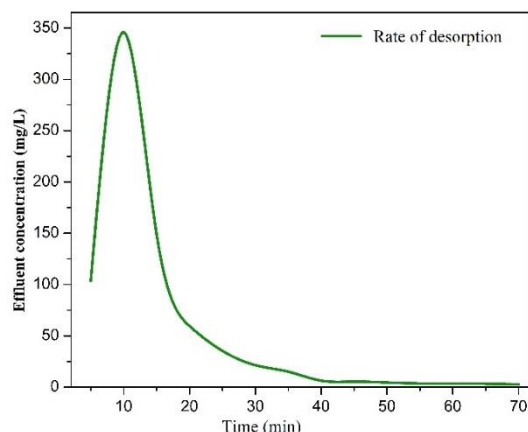


Fig 9. Rate of desorption of FeAl(BDC) MOF in a column mode in regeneration study.

4. Conclusion

In the study reported, a bimetallic FeAl(BDC) MOF was synthesized and characterized. Its adsorption potential towards Rhodamine B dye was examined in the batch and unique hybrid adsorbent-sand column. Following are the significant outcomes of this study:

- The maximum uptake capacity of FeAl(BDC) MOF in optimized conditions for batch study (pH = 5.36±0.2, stirring speed = 200±20, temperature = 30 °C, adsorbent mass = 1.0 g/L, RhB concentration = 25 mg/L) was 41.86 mg/g.
- The adsorption of RhB dye was spontaneous and endothermic in nature, followed Pseudo second-order kinetics and Freundlich isotherm model.
- In the fixed-bed column study, the breakthrough was achieved in 13 hours with the effective treated volume of 8700 mL and MTZ of 2.05 cm. In addition, % removal of RhB dye in optimized conditions (flow rate = 5 mL/min, bed height = 13 cm, adsorbent mass = 1 g, RhB concentration = 20 mg/L) was 64%.
- The nonlinear kinetic models fitted with column study data depicted high correlation ($R^2 = 0.975-0.998$), and the experimental adsorption capacity (q_{exp}) of 113.05 mg/g, was found similar to calculated adsorption capacity (q_{cal}) of Thomas and D-R's 114.94 mg/g and 113.41 mg/g, respectively.
- The BDST model also shows a good fitting with the BTC, which is the suitable template to scale up the fixed-bed columns into possible filtration units.

Furthermore, the study also draws attention to the potential application of sand-FeAl(BDC) based filters, etc., having various water treatment and filtration applications in various parts of the world, particularly having economically poor communities subjected to such pollutants. Hence, it is concluded that the as developed river sand-FeAl(BDC) has the potential to treat multiple dyes (MB, MG, CV, RhB, MO) in

555 continuous system and can also be utilized to treat polluted water with alike
556 contaminations.

557

558

559 **Reference**

- 560 Abdi J, Abedini H (2020) MOF-based polymeric nanocomposite beads as an efficient
561 adsorbent for wastewater treatment in batch and continuous systems: Modelling and
562 experiment. *Chem Eng J*. doi: 10.1016/j.cej.2020.125862
- 563 Afroze S, Sen TK, Ang HM (2016) Adsorption performance of continuous fixed bed column
564 for the removal of methylene blue (MB) dye using *Eucalyptus sheathiana* bark biomass.
565 *Res Chem Intermed*. doi: 10.1007/s11164-015-2153-8
- 566 Ai L, Zhang C, Li L, Jiang J (2014) Iron terephthalate metal-organic framework: Revealing
567 the effective activation of hydrogen peroxide for the degradation of organic dye under
568 visible light irradiation. *Appl Catal B Environ*. doi: 10.1016/j.apcatb.2013.10.056
- 569 Aksu Z, Tezer S (2005) Biosorption of reactive dyes on the green alga *Chlorella vulgaris*.
570 *Process Biochem*. doi: 10.1016/j.procbio.2004.06.007
- 571 Amini M, Arami M, Mahmoodi NM, Akbari A (2011) Dye removal from colored textile
572 wastewater using acrylic grafted nanomembrane. *Desalination*. doi:
573 10.1016/j.desal.2010.09.014
- 574 Amirilargani M, Merlet RB, Hedayati P, et al (2019) MIL-53(Al) and NH₂-MIL-53(Al)
575 modified α -alumina membranes for efficient adsorption of dyes from organic solvents.
576 *Chem Commun*. doi: 10.1039/c9cc01624d
- 577 Babazadeh M, Abolghasemi H, Esmaeili M, et al (2021) Comprehensive batch and
578 continuous methyl orange removal studies using surfactant modified chitosan-
579 clinoptilolite composite. *Sep Purif Technol*. doi: 10.1016/j.seppur.2021.118601
- 580 Banerjee A, Gokhale R, Bhatnagar S, et al (2012) MOF derived porous carbon-Fe₃O₄
581 nanocomposite as a high performance, recyclable environmental superadsorbent. *J*
582 *Mater Chem* 22:19694–19699. doi: 10.1039/c2jm33798c
- 583 Botas JA, Calleja G, Sánchez-Sánchez M, Orcajo MG (2010) Cobalt doping of the MOF-5
584 framework and its effect on gas-adsorption properties. *Langmuir*. doi:
585 10.1021/la100423a
- 586 Chakraborty G, Park IH, Medishetty R, Vittal JJ (2021) Two-Dimensional Metal-Organic
587 Framework Materials: Synthesis, Structures, Properties and Applications. *Chem. Rev.*

588 121:

589 Charumathi D, Das N (2012) Packed bed column studies for the removal of synthetic dyes
590 from textile wastewater using immobilised dead *C. tropicalis*. *Desalination*. doi:
591 10.1016/j.desal.2011.09.023

592 Chatterjee A, Jana AK, Basu JK (2021) Silica supported binary metal organic framework for
593 removing organic dye involving combined effect of adsorption followed by
594 photocatalytic degradation. *Mater Res Bull*. doi: 10.1016/j.materresbull.2021.111227

595 Chegeni M, Mehri M, Dehdashtian S (2021) Photocatalytic bauxite and red mud/graphitic
596 carbon nitride composites for Rhodamine B removal. *J Mol Struct*. doi:
597 10.1016/j.molstruc.2021.130752

598 Chen AH, Chen SM (2009) Biosorption of azo dyes from aqueous solution by
599 glutaraldehyde-crosslinked chitosans. *J Hazard Mater*. doi:
600 10.1016/j.jhazmat.2009.07.104

601 Cheng ZL, Li Y xiang, Liu Z (2018) Study on adsorption of rhodamine B onto Beta zeolites
602 by tuning SiO₂/Al₂O₃ ratio. *Ecotoxicol Environ Saf*. doi: 10.1016/j.ecoenv.2017.11.005

603 Choudhary V, Patel M, Pittman CU, Mohan D (2020) Batch and Continuous Fixed-Bed Lead
604 Removal Using Himalayan Pine Needle Biochar: Isotherm and Kinetic Studies. *ACS*
605 *Omega* 5:16366–16378. doi: 10.1021/acsomega.0c00216

606 Cruz-Olivares J, Pérez-Alonso C, Barrera-Díaz C, et al (2013) Modeling of lead (II)
607 biosorption by residue of allspice in a fixed-bed column. *Chem Eng J*. doi:
608 10.1016/j.cej.2013.04.101

609 Dąbrowski A (2001) Adsorption - From theory to practice. *Adv. Colloid Interface Sci*. 93:

610 Du JJ, Yuan YP, Sun JX, et al (2011) New photocatalysts based on MIL-53 metal-organic
611 frameworks for the decolorization of methylene blue dye. *J Hazard Mater*. doi:
612 10.1016/j.jhazmat.2011.04.029

613 Gaaz TS, Sulong AB, Akhtar MN, et al (2015) Properties and applications of polyvinyl
614 alcohol, halloysite nanotubes and their nanocomposites. *Molecules* 20:22833–22847.
615 doi: 10.3390/molecules201219884

616 Gangu KK, Maddila S, Mukkamala SB, Jonnalagadda SB (2016) A review on contemporary
617 Metal-Organic Framework materials. *Inorganica Chim. Acta*

618 Geetha Malini PS, Durgadevi P, Senthil Kumar N, Rani S (2020) Synthesis and
619 characterisation of CdO nanoparticles: An efficient nanomaterial for the removal of
620 Rhodamine B. *Mater Today Proc*. doi: 10.1016/j.matpr.2020.07.689

621 Gupta VK, Suhas (2009) Application of low-cost adsorbents for dye removal - A review. *J.*

622 Environ. Manage. 90:
623 Han R, Ding D, Xu Y, et al (2008) Use of rice husk for the adsorption of congo red from
624 aqueous solution in column mode. *Bioresour Technol.* doi:
625 10.1016/j.biortech.2007.06.027
626 Jiao Y, Pei J, Chen D, et al (2017) Mixed-metallic MOF based electrode materials for high
627 performance hybrid supercapacitors. *J Mater Chem A.* doi: 10.1039/C6TA09805C
628 Joseph L, Jun BM, Jang M, et al (2019) Removal of contaminants of emerging concern by
629 metal-organic framework nanoadsorbents: A review. *Chem. Eng. J.*
630 Kadirvelu K, Karthika C, Vennilamani N, Pattabhi S (2005) Activated carbon from industrial
631 solid waste as an adsorbent for the removal of Rhodamine-B from aqueous solution:
632 Kinetic and equilibrium studies. *Chemosphere.* doi: 10.1016/j.chemosphere.2005.01.047
633 Karami A, Sabouni R, Al-Sayah MH, Aidan A (2021) Adsorption potentials of iron-based
634 metal-organic framework for methyl orange removal: batch and fixed-bed column
635 studies. *Int J Environ Sci Technol.* doi: 10.1007/s13762-020-03103-2
636 Kiran I, Akar T, Ozcan AS, et al (2006) Biosorption kinetics and isotherm studies of Acid
637 Red 57 by dried *Cephalosporium aphidicola* cells from aqueous solutions. *Biochem Eng*
638 *J.* doi: 10.1016/j.bej.2006.07.008
639 Lellis B, Fávaro-Polonio CZ, Pamphile JA, Polonio JC (2019) Effects of textile dyes on
640 health and the environment and bioremediation potential of living organisms. *Biotechnol*
641 *Res Innov.* doi: 10.1016/j.biori.2019.09.001
642 Li C, Xiong Z, Zhang J, Wu C (2015) The Strengthening Role of the Amino Group in Metal-
643 Organic Framework MIL-53 (Al) for Methylene Blue and Malachite Green Dye
644 Adsorption. *J Chem Eng Data.* doi: 10.1021/acs.jced.5b00692
645 Li FL, Wang P, Huang X, et al (2019a) Large-Scale, Bottom-Up Synthesis of Binary Metal-
646 Organic Framework Nanosheets for Efficient Water Oxidation. *Angew Chemie - Int Ed.*
647 doi: 10.1002/anie.201902588
648 Li J, Bhatt PM, Li J, et al (2020) Recent Progress on Microfine Design of Metal-Organic
649 Frameworks: Structure Regulation and Gas Sorption and Separation. *Adv. Mater.* 32:
650 Li J, Huang W, Wang M, et al (2019b) Low-Crystalline Bimetallic Metal-Organic
651 Framework Electrocatalysts with Rich Active Sites for Oxygen Evolution. *ACS Energy*
652 *Lett.* doi: 10.1021/acscenergylett.8b02345
653 Li Z, Meng X, Zhang Z (2019c) Equilibrium and kinetic modelling of adsorption of
654 Rhodamine B on MoS₂. *Mater Res Bull.* doi: 10.1016/j.materresbull.2018.11.012
655 Lu Q, Gao W, Du J, et al (2012) Discovery of environmental rhodamine B contamination in

656 paprika during the vegetation process. *J Agric Food Chem.* doi: 10.1021/jf300067z

657 Masoomi MY, Morsali A, Dhakshinamoorthy A, Garcia H (2019) Mixed-Metal MOFs:
658 Unique Opportunities in Metal–Organic Framework (MOF) Functionality and Design.
659 *Angew. Chemie - Int. Ed.* 58:

660 Mishra P, Uppara HP, Mandal B, Gumma S (2014) Adsorption and separation of carbon
661 dioxide using MIL-53(Al) metal-organic framework. In: *Industrial and Engineering*
662 *Chemistry Research.*

663 Mon M, Bruno R, Ferrando-Soria J, et al (2018) Metal-organic framework technologies for
664 water remediation: Towards a sustainable ecosystem. *J. Mater. Chem. A*

665 Nagaraja R, Kottam N, Girija CR, Nagabhushana BM (2012) Photocatalytic degradation of
666 Rhodamine B dye under UV/solar light using ZnO nanopowder synthesized by solution
667 combustion route. *Powder Technol.* doi: 10.1016/j.powtec.2011.09.014

668 Nazir MA, Bashir MS, Jamshaid M, et al (2021) Synthesis of porous secondary metal-doped
669 MOFs for removal of Rhodamine B from water: Role of secondary metal on efficiency
670 and kinetics. *Surfaces and Interfaces.* doi: 10.1016/j.surfin.2021.101261

671 Podder MS, Majumder CB (2016) Fixed-bed column study for As(III) and As(V) removal
672 and recovery by bacterial cells immobilized on Sawdust/MnFe₂O₄ composite. *Biochem*
673 *Eng J.* doi: 10.1016/j.bej.2015.09.008

674 Postai DL, Demarchi CA, Zanatta F, et al (2016) Adsorption of rhodamine B and methylene
675 blue dyes using waste of seeds of *Aleurites Moluccana*, a low cost adsorbent. *Alexandria*
676 *Eng J.* doi: 10.1016/j.aej.2016.03.017

677 Pu M, Guan Z, Ma Y, et al (2018) Synthesis of iron-based metal-organic framework MIL-53
678 as an efficient catalyst to activate persulfate for the degradation of Orange G in aqueous
679 solution. *Appl Catal A Gen.* doi: 10.1016/j.apcata.2017.09.021

680 Qian X, Yadian B, Wu R, et al (2013) Structure stability of metal-organic framework MIL-53
681 (Al) in aqueous solutions. *Int J Hydrogen Energy* 38:16710–16715. doi:
682 10.1016/J.IJHYDENE.2013.07.054

683 Rathour RKS, Bhattacharya J, Mukherjee A (2020) Selective and multicycle removal of
684 Cr(VI) by graphene oxide–EDTA composite: Insight into the removal mechanism and
685 ionic interference in binary and ternary associations. *Environ Technol Innov.* doi:
686 10.1016/j.eti.2020.100851

687 Richardson SD, Willson CS, Rusch KA (2004) Use of rhodamine water tracer in the
688 marshland upwelling system. *Ground Water.* doi: 10.1111/j.1745-6584.2004.tb02722.x

689 Robinson T, McMullan G, Marchant R, Nigam P (2001) Remediation of dyes in textile

690 effluent: A critical review on current treatment technologies with a proposed alternative.
691 Bioresour Technol. doi: 10.1016/S0960-8524(00)00080-8

692 Saha P Das, Chakraborty S, Chowdhury S (2012) Batch and continuous (fixed-bed column)
693 biosorption of crystal violet by *Artocarpus heterophyllus* (jackfruit) leaf powder.
694 Colloids Surfaces B Biointerfaces. doi: 10.1016/j.colsurfb.2011.11.057

695 Saini RD (2017) Textile Organic Dyes: Polluting effects and Elimination Methods from
696 Textile Waste Water.

697 Seth S, Matzger AJ (2017) Metal-Organic Frameworks: Examples, Counterexamples, and an
698 Actionable Definition. Cryst. Growth Des.

699 Tiwari MK, Bajpai S, Dewangan UK, Tamrakar RK (2015) Assessment of heavy metal
700 concentrations in surface water sources in an industrial region of central India. Karbala
701 Int J Mod Sci. doi: 10.1016/j.kijoms.2015.08.001

702 Vu TA, Le GH, Dao CD, et al (2015) Arsenic removal from aqueous solutions by adsorption
703 using novel MIL-53(Fe) as a highly efficient adsorbent. RSC Adv. doi:
704 10.1039/c4ra12326c

705 Wang J, Guo X (2020a) Adsorption kinetic models: Physical meanings, applications, and
706 solving methods. J. Hazard. Mater. 390:

707 Wang J, Guo X (2020b) Adsorption isotherm models: Classification, physical meaning,
708 application and solving method. Chemosphere 258:

709 Wang X, Guo Y, Jia Z, et al (2021) Fabrication of graphene oxide/polydopamine adsorptive
710 membrane by stepwise in-situ growth for removal of rhodamine B from water.
711 Desalination. doi: 10.1016/j.desal.2021.115220

712 Weber TW, Chakravorti RK (1974) Pore and solid diffusion models for fixed-bed adsorbers.
713 AIChE J. doi: 10.1002/aic.690200204

714 Wu Q, Siddique MS, Guo Y, et al (2021) Low-crystalline bimetallic metal-organic
715 frameworks as an excellent platform for photo-Fenton degradation of organic
716 contaminants: Intensified synergism between hetero-metal nodes. Appl Catal B Environ.
717 doi: 10.1016/j.apcatb.2021.119950

718 Yadav S, Tyagi DK (2011) Equilibrium and Kinetic Studies on Adsorption of Aniline Blue
719 From Aqueous Solution Onto Rice Husk Carbon.

720 Yaghi OM, O'Keeffe M, Ockwig NW, et al (2003) Reticular synthesis and the design of new
721 materials. Nature

722 Yan J, Jiang S, Ji S, et al (2015) Metal-organic framework MIL-53(Al): Synthesis, catalytic
723 performance for the Friedel-Crafts acylation, and reaction mechanism. Sci China Chem.

724 doi: 10.1007/s11426-015-5359-0

725 Zaheer Z, AL-Asfar A, Aazam ES (2019) Adsorption of methyl red on biogenic Ag@Fe
726 nanocomposite adsorbent: Isotherms, kinetics and mechanisms. J Mol Liq. doi:
727 10.1016/j.molliq.2019.03.030

728 Zarenezhad M, Zarei M, Ebratkhahan M, Hosseinzadeh M (2021) Synthesis and study of
729 functionalized magnetic graphene oxide for Pb²⁺ removal from wastewater. Environ
730 Technol Innov. doi: 10.1016/j.eti.2021.101384

731

732 **Statements & Declarations**

733 **Compliance with Ethical Standards**

734 Not applicable

735 **Consent to Participate**

736 Not applicable

737 **Consent to Publish**

738 Not applicable

739 **Funding**

740 All the author thanks the School of Environmental Science and Engineering and Central
741 Research Facility at IIT, Kharagpur for the technical and material support, space and
742 instrumentation to carry out this work. Also, H Singh, S Raj, and Dr. RKS Rathour sincerely
743 appreciate the Ministry of Human Resource Development, Government of India, for their
744 PhD. Fellowships.

745 **Competing Interests**

746 The authors have no competing interests to declare that are relevant to the content of this
747 article.

748 **Author Contributions**

749 All the authors' contribution has been acknowledged as mentioned. Hemant Singh:
750 Conceptualization, Methodology, Software, Data curation, writing original-draft,

751 visualization and Investigation. Sankalp Raj: Assistance to Investigation. Rishi Karan Singh
752 Rathour: Assistance to Investigation, Writing–review & editing. Jayanta Bhattacharya:
753 Assistance to Investigation, Supervision, Writing–review & editing.

754 **Data Availability**

755 All the relevant experimental data are within the manuscript.

756